Low-energy Properties of Electrons and Holes in CuFeS$_2$

Bjørnulf Brekke,[1] Roman Malyshev,[2] Ingeborg-Helene Svenum,[3, 4] Sverre
M. Selbach,[5] Thomas Tybell,[2] Christoph Brüne,[1] and Arne Brataas[1]

[1] *Center for Quantum Spintronics, Department of Physics,*
NTNU - Norwegian University of Science and Technology, NO-7491 Trondheim, Norway
[2] *Department of Electronic Systems, NTNU - Norwegian University of Science and Technology, NO-7491 Trondheim, Norway*
[3] *Department of Chemical Engineering, NTNU - Norwegian University of Science and Technology, NO-7491 Trondheim, Norway*
[4] *SINTEF Industry, NO-7465 Trondheim, Norway*
[5] *Department of Materials Science and Engineering,*
NTNU - Norwegian University of Science and Technology, NO-7491 Trondheim, Norway
(Dated: February 17, 2023)

The antiferromagnetic semiconductor CuFeS$_2$ belongs to a magnetic symmetry class that is of interest for spintronics applications. In addition, its crystal lattice is compatible with Si, making it possible to integrate it with non-magnetic semiconducting structures. Therefore, we investigate this material by finding the effective $\boldsymbol{k} \cdot \boldsymbol{p}$ Hamiltonian for the electron- and hole bands. We base this description on *ab initio* calculations and classify the electronic bands by their symmetry. As a result, we find that CuFeS$_2$ exhibits spin-polarized bands. We also find that the crystal symmetry allows for the anomalous Hall effect. Finally, we suggest using cyclotron resonance to verify our proposed effective mass tensors at the conduction band minimum and valence band maximum.

I. INTRODUCTION

Antiferromagnets currently attract considerable interest because of their intriguing ultrafast spin dynamics that couple to electric currents [1–3]. The interplay between spin excitations and the transport of spin, heat, and charge can reveal novel phenomena. Recent works have demonstrated the central capabilities of antiferromagnets for use in spintronics devices. Electrical currents can switch the staggered field in antiferromagnets [4–6]. Spins can propagate longer than micrometers in antiferromagnetic insulators [7]. Dynamical spins in antiferromagnets can act as spin batteries, as revealed via the inverse spin Hall effect [8–14]. These features, the high-frequency capacity, and the robustness against external magnetic fields can enable new ways to realize high-speed electronics.

Magnetic semiconductors are of interest for use in spintronics devices because of the tunable charge carrier density, integration with other semiconductors such as Si and GaAs, and the possibility of creating low-dimensional structures like quantum wells, quantum wires, and quantum dots. Decades ago, dilute ferromagnetic semiconductors got attention because of the prospect of combined control of the electron spin and the charge carriers [15–17]. Materials like GaMnAs exhibit a reasonably high Curie temperature of around 200 K, yet it is significantly below room temperature. (In,Fe)As is an electron-induced ferromagnetic semiconductor with a Curie temperature above 300 K [17].

On the other hand, antiferromagnetic semiconductors are underexplored for use in spintronics devices. This class of materials combines ultra-fast spin dynamics and tunable electron- and hole properties that potentially can enable new features and reveal interesting phenomena. CuFeS$_2$ is a good candidate because of its high Néel temperature of 823 K [18]. Additionally, its magnetic crystal structure belongs to an intriguing symmetry class. This is the type I Shubnikov class, and it generally allows for the anomalous Hall effect and spin-polarized electron bands [19, 20]. These properties are typical for ferromagnets. In this sense, CuFeS$_2$ may exhibit favorable properties of both ferro- and antiferromagnets. To make use of its semiconducting properties, CuFeS$_2$ can also be integrated with Si due to their compatible lattice structures [21].

CuFeS$_2$ has already seen interest in different areas, mostly due to its thermoelectric properties [22–28]. However, to understand its semiconductor properties, knowledge and models of the dispersions of electrons and holes at low doping levels are essential. Previous works compute, with *ab initio* techniques, the electronic band structure [29–31]. However, future exploration of this antiferromagnetic semiconductor requires a systematic study of the low-energy electron and hole properties while taking spin-orbit coupling into account. The purpose of the present paper is to fill this knowledge gap.

The paper is organized as follows. First, we provide a brief overview of the magnetic space group (MSG) symmetries of CuFeS$_2$. We use the MSG symmetries to give a phenomenological description of the conductivity tensor based on Neumann's principle. The following section presents *ab initio* calculations of the electronic bands and the symmetry characterization of the principal bands relevant for electron- and hole transport. We then derive effective models for the valence band maximum and conduction band minimum based on this symmetry classification. Lastly, we discuss how electron cyclotron resonance can be used to verify the suggested electron- and hole-band extrema and dispersions.
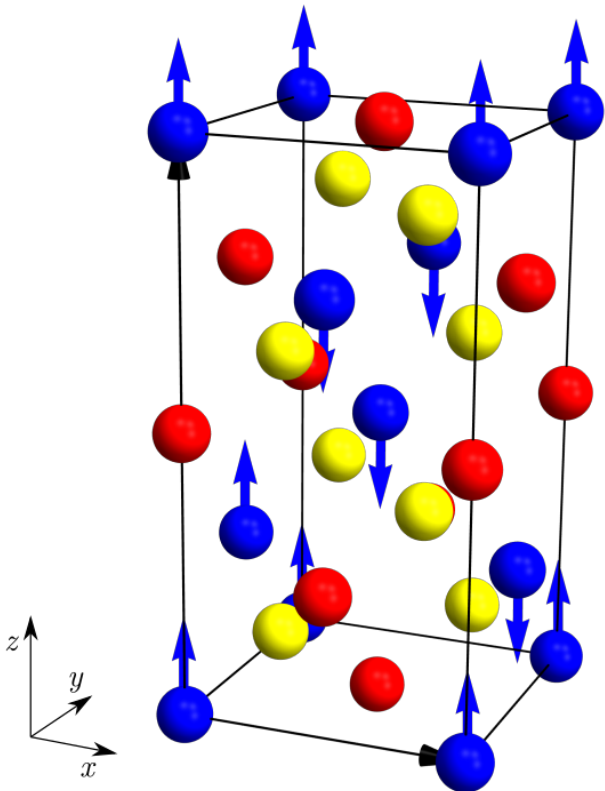
FIG. 1. The conventional unit cell of CuFeS$_2$. The Fe-atoms are blue and host magnetic moments represented by arrows, the Cu-atoms are red, and the S-atoms are yellow.

II. CRYSTAL SYMMETRY

Chalcopyrite, CuFeS$_2$ has a tetragonal crystal structure with space group $I\bar{4}2d$, #122 [32]. To account for the collinear antiferromagnetic ground state, we consider its magnetic space group [33]. This configuration is shown in Figure 1. The magnetic space group is a type I Shubnikov group, also called a Fedorov group. Such groups lack anti-unitary symmetry operations such as time-reversal symmetry. In other words, the crystal space group and the magnetic space group are isomorphic. Consequently, the chemical and the magnetic unit cell coincide. The MSG consists of the eight symmetries

$$(E|0), \quad (C_{2z}|0), \quad (S_{4z}^+|0), \quad (S_{4z}^-|0), \quad \text{(1a)}$$

$$(C_{2x}|\boldsymbol{\tau}), \quad (C_{2y}|\boldsymbol{\tau}), \quad (\sigma_{xy}|\boldsymbol{\tau}), \quad (\sigma_{\bar{x}y}|\boldsymbol{\tau}), \quad \text{(1b)}$$

where the origin of the unit cell coincides with a Fe ion. Four of the symmetries are non-symmorphic symmetry operations. They are composite symmetries consisting of a point group operation and a translation $\boldsymbol{\tau} = (0, a/2, c/4)$ in terms of the tetragonal lattice constants a and c. The crystal is non-centrosymmetric such that the space group allows for antiferromagnetic

skyrmions [34]. The non-symmorphic symmetries relate the spins of the two Fe atoms and render chalcopyrite a fully compensated antiferromagnet (AFM). The fact that the oppositely aligned spins are related by unitary non-symmorphic symmetries allows for interesting features for spintronic applications. According to the classification given by Yuan *et al.* [19], the MSG allows for AFM-induced spin-polarized electron bands. We investigate this phenomenon further in section IV. B. along with *ab initio* calculations.

III. ELECTRON CONDUCTIVITY

CuFeS2 becomes conducting when it is electron- or hole doped. In this case, the conductivity σ captures the electron transport properties of the crystal. We consider the conductivity to first order in the Néel vector

$$J_i = \sigma_{ij} E_j + \sigma_{ijk} E_j n_k. \quad \text{(2)}$$

Here, i, j, and k refer to Cartesian directions of the current density J_i, the electric field E_j, and the Néel vector n_k. The first term on the right-hand side includes the second-rank conductivity tensor σ_{ij}. The second term is proportional to n_k and yields a third-rank conductivity tensor σ_{ijk}. Notably, any anomalous Hall conductivity vanishes for conventional collinear AFMs. That is, AFMs with either a composite time-reversal- and inversion symmetry or time-reversal- and translation symmetry [20]. CuFeS$_2$ has neither of these composite symmetries, which opens the possibility for a finite anomalous Hall effect.

The MSG symmetries allow for a phenomenological description of the conductivity tensors using Neumann's principle [35]. We require σ_{ij} and σ_{ijk} to be invariant under all symmetries

$$\sigma_{ij} = \mathcal{R}_{ii'}\mathcal{R}_{jj'}\sigma_{i'j'}, \quad \text{(3a)}$$

$$\sigma_{ijk} = (-1)^{l+m}\mathcal{R}_{ii'}\mathcal{R}_{jj'}\mathcal{R}_{kk'}\sigma_{i'j'k'}. \quad \text{(3b)}$$

The Néel vector n_k has special transformation properties. It is a pseudovector which means it is invariant under orientation reversal. Also, it changes sign under sublattice exchange caused by the non-symmorphic transformations. To account for this, we introduce the boolean variables $l, m \in \{0, 1\}$, which are non-zero for orientation-reversing- and non-symmorphic symmetries, respectively.

As a result, the conductivity relations to the first order in $\boldsymbol{n}$ are

$$J_x = \sigma_t E_x + \sigma_t' E_x n_z + \sigma_A' E_z n_x, \quad \text{(4a)}$$
$$J_y = \sigma_t E_y + \sigma_t' E_y n_z + \sigma_A' E_z n_y, \quad \text{(4b)}$$
$$J_z = \sigma_l E_z + \sigma_l' E_z n_z + \sigma_B'(E_x n_x + E_y n_y). \quad \text{(4c)}$$

The coefficients $\sigma_t, \sigma_l, \sigma_l', \sigma_t', \sigma_A'$ and σ_B' can be found empirically or from microscopic calculations. In each of

the relations, the first term corresponds to a Nèel vector-independent diagonal conductivity. The second term is a shift in the diagonal conductivity dependent on the direction of the Nèel vector to linear order. The last terms are off-diagonal conductivity terms corresponding to an anomalous Hall effect. These are finite when the Nèel vector takes on an x- or y- component. The relations in Eq. (4) allow for direct measurement of both the sign and direction of the Néel vector. In the following, we consider the electron structure properties using *ab initio* calculations.

IV. AB-INITIO CALCULATIONS

A. Methods

Density functional theory (DFT) calculations were performed with the projected augmented-wave method [36, 37]. Accordingly, we used the Vienna *Ab Initio* Simulation Package (VASP) in the DFT+U methodology, including spin-orbit coupling (SOC), to capture the SOC-induced band splitting at high-symmetry points. To represent the bulk crystal, we used a periodic model of a single conventional unit cell that contains 16 atoms. Furthermore, we sampled the Brillouin zone using a Γ-centered mesh with at least $4 \times 4 \times 2$ k-points. The mesh was generated with the Monkhorst-Pack scheme [38]. For the density of states (DOS) calculations, we changed the k-mesh to include $12 \times 12 \times 6$ k-points. The electron band structure was sampled at 100 k-points on the interval between each pair of high-symmetry points on the $\boldsymbol{k}$-path. We set an energy cut-off at 700 eV.

To relax the structure and minimize the total energy, we applied the iterative conjugate-gradient method. We relaxed the atomic positions until the residual forces acting on the atoms were smaller than 10^{-5} eV/Å and the energy difference in the final convergence step was smaller than 10^{-8} eV per unit cell.

The Fe magnetic moments converged to consistent values for initial inputs on the interval 1 to 6 Bohr magnetons μ_B. The spins are oriented antiferromagnetically, as illustrated in Figure 1. We considered other collinear AFM orderings, as well as a ferromagnetically ordered structure. In consistence with the results of Ref. [27], and as shown in Appendix A, these orderings produced a higher energy state than the chosen AFM structure.

The DFT+U scheme of Dudarev *et al.* [40] was used, with a varying U_{eff} applied to Fe $3d$ and a $U_{\text{eff}} = 0.1$ eV applied to Cu $3d$. We used the Perdew-Burke-Ernzerhof functional for solids (PBEsol) [41] for the relaxation, electronic structure, density of states, and band structure calculations. The states $3s^2 3p^4$, $3p^6 4s^1 3d^{10}$ and $3p^6 4s^1 3d^7$ were treated as valence electrons for the atomic types S, Cu, and Fe, respectively. To determine a fitting value of U_{eff} in DFT+U, we performed a full relaxation with the HSE06 hybrid functional [42]. Table I presents the results from the PBEsol relaxations with
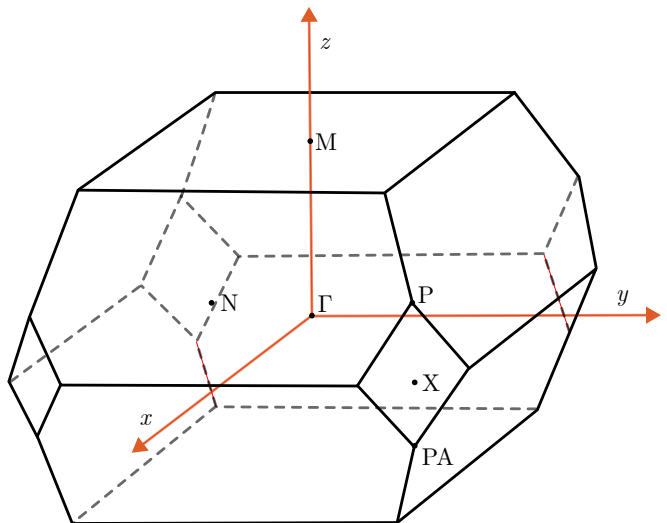
FIG. 2. The first Brillouin zone of $CuFeS_2$ with high-symmetry points. The coordinate system denotes the direction of the crystal momenta.
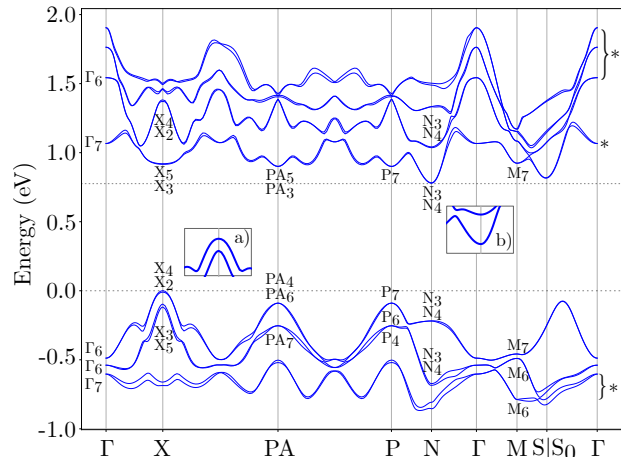
FIG. 3. The electronic band structure of $CuFeS_2$ with spin-orbit coupling. The bands are classified by irreducible representations at the high-symmetry points according to the notation in Ref. [39]. Isolated bands marked by an asterisk have a non-trivial topological index. The insets show the VBM a) and CBM b) in the absence of SOC.

various U_{eff} values applied to Fe $3d$ orbitals, as well as those determined with the HSE06 functional. We fit the U_{eff} value to the first lattice constant, a, and calculated the DOS and band structure with $U_{\text{eff}} = 4.7$. This value gives the lattice constants $a = 5.259$ Å and $c = 10.407$ Å.

B. Results

Figure 3 shows the calculated electronic band structure. The bands follow a path in $\boldsymbol{k}$-space traversing the
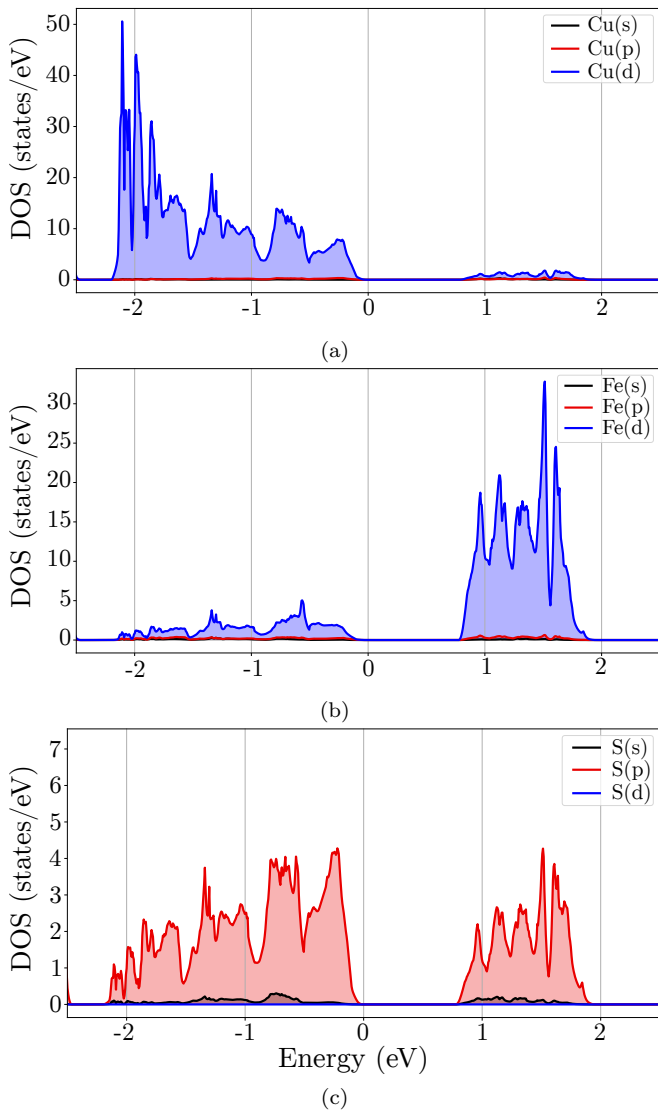
FIG. 4. The atom-decomposed density of state from *ab initio* calculations of CuFeS$_2$. The Cu 3d- and S 3p orbitals dominate the valence band, whereas the Fe 3d- and S 3p orbitals dominate the conduction band. The scaling on the y-axes differs for better visibility.

high-symmetry points denoted in Table II and shown in Figure 2. The electron states at the high-symmetry points transform as irreducible representations of the corresponding little group. The full set of irreps, for each of the high symmetry points, is given in Ref. [39]. Consistent with other *ab initio* calculations [23], the band structure is strongly anisotropic. The valence band maximum (VBM) is at the X-point, and the conduction band minimum (CBM) is at the N-point. The X-point is part of a two-fold valley structure, and the N-point is part of a four-fold valley structure. This renders chalcopyrite a multivalley semiconductor. The bands show an indirect band gap of 0.779 eV. Experimentally, values between 0.3-0.6 eV have been reported [43, 44]. The direct band gap is 0.915 eV and found at the X-point.

In the presence of SOC, the VBM and CBM exhibit band splittings. However, the bands are degenerate in the absence of SOC, as shown by the insets of Figure 3. However, in the presence of a magnetic ordering, this band degeneracy is not symmetry protected. Moreover, based on the form of the basis functions presented in section V. A and B, the splittings at the X- and N-points are not solely due to SOC. Hence, the band splittings should be interpreted as a result of the interplay of SOC and the magnetic crystal.

Figure 4 shows the atom-decomposed electron density of states. Cu- and S electrons dominate the valence band. On the other hand, the conduction bands are dominated by Fe- and S electrons. These findings suggest that conduction band electrons are more strongly coupled to the localized magnetic moments than the valence band electrons are. Hence, the spin polarization of the conduction band is of special interest.

Because the sublattice spins of CuFeS$_2$ are related by non-symmorphic symmetries instead of composite time-reversal and inversion symmetry, its magnetic symmetry class allows for spin-polarized electron bands. Figure 5 shows the net spin projected density of states for the two lowest conduction bands on the considered $\boldsymbol{k}$-path based on the *ab initio* calculations. At specific points, the crystal symmetries prohibit spin-polarizations in all directions. This is the case for the Γ-, X-, PA-, P-, and M-point, as well as for some high-symmetry lines. Notably, the CBM at the N-point exhibits a finite spin-polarization in the y-direction. The spin polarization of the related valley N$'$ has an opposite sign. There is a similar relationship between N$''$ and N$'''$ with spin polarization in the x-direction.

Spin polarization in the z-direction is more restricted by symmetry. Any high-symmetry point or -line with a symmetry listed in Eq. (1b) as part of its little group is prohibited from having spin-polarized bands. The reason is that these symmetry operations relate the two magnetic sublattices. For the chosen $\boldsymbol{k}$-path, only the N-Γ

TABLE I. Lattice parameters a, c, their ratio c/a and magnetic moment of Fe atoms for DFT+U models using PBEsol with different U_{eff} values for Fe 3d. The bottom row shows the same quantities calculated with the hybrid functional HSE06 for comparison.

U_{eff} (eV)	a (Å)	c (Å)	c/a	m_s (μ_B)
0	5.152	10.177	1.975	2.620
1	5.196	10.225	1.968	3.127
2	5.218	10.285	1.971	3.335
3	5.236	10.337	1.974	3.487
4	5.251	10.380	1.977	3.607
5	5.263	10.416	1.979	3.709
6	5.275	10.442	1.980	3.801
7	5.301	10.420	1.966	3.883
8	5.305	10.473	1.974	3.966
9	5.288	10.571	1.999	4.051
HSE06	5.259	10.366	1.971	3.715
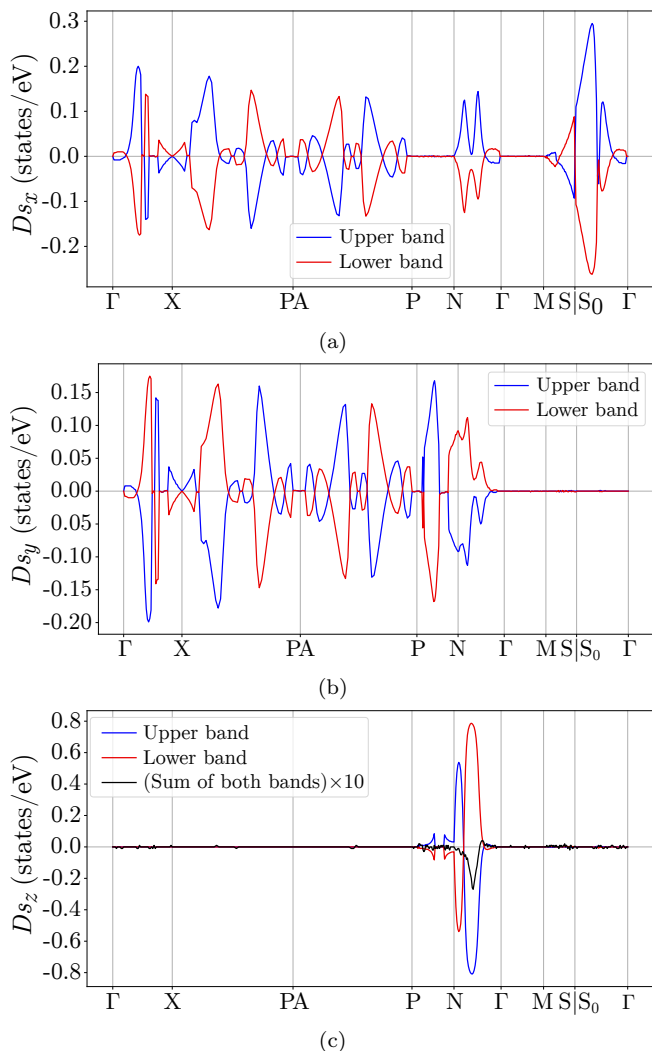
FIG. 5. The net spin projected density of states Ds_i in the (a) $i = x$-, (b) $i = y$- and (c) $i = z$ -direction of the two lowest electron conduction bands. The numerical results are consistent with the crystal symmetry, except for the partly finite spin polarization in the z-direction on the P-N interval.

interval lack these symmetries. Although this interval is a small part of this specific $\boldsymbol{k}$-path, it represents most of the Brillouin zone in the sense that its little group contains the identity operation only. Hence, we expect a large part of the Brillouin zone to exhibit electron bands spin-polarized in the z- direction as well as the x- and y-direction.

Large efforts have been made to determine the topological character of magnetic compounds. We consider the electron bands of $CuFeS_2$ with respect to the symmetry-based indicator as introduced in Ref. [45]. For the magnetic space of $CuFeS_2$, it is a $\mathbb{Z}_2$ topological invariant [46]. Based on the *ab initio* calculations and magnetic quantum chemistry software [47, 48], we find that certain bands of $CuFeS_2$ are topologically non-trivial with respect to this topological invariant. These isolated bands

are marked by an asterisk in Figure 3. The total topological index summed over all occupied bands is zero. Hence, the *ab initio* calculations and the crystal symmetries suggest that $CuFeS_2$ does not exhibit topologically protected edge states.

V. EFFECTIVE MASS THEORY

In this section, we develop an effective theory for the band structure of the CBM and VBM. To that end, we use $\boldsymbol{k} \cdot \boldsymbol{p}$ theory [49–52].

We start with the Hamiltonian

$$\mathcal{H} = \frac{p^2}{2m} + V(\boldsymbol{r}) + \frac{\hbar}{2m^2c^2}(\nabla V(\boldsymbol{r}) \times \boldsymbol{p}) \cdot \boldsymbol{\sigma}, \quad (5)$$

where $\boldsymbol{p}$ is the momentum operator and m is the electron mass. The crystal potential $V(\boldsymbol{r})$ gives rise to SOC. The SOC term contains the spin Pauli matrices $\boldsymbol{\sigma}$.

Following the standard approach, we let the Hamiltonian in Eq. (5) act on Bloch waves $\psi_{n\boldsymbol{k}}(\boldsymbol{r}) = e^{i\boldsymbol{\kappa}\cdot\boldsymbol{r}}\left(e^{i\boldsymbol{k}_0\cdot\boldsymbol{r}}u_{n\boldsymbol{k}_0}(\boldsymbol{r})\right)$, where the wave function $u_{n\boldsymbol{k}_0}(\boldsymbol{r})$ has the lattice periodicity. The crystal momentum $\boldsymbol{k} = \boldsymbol{k}_0 + \boldsymbol{\kappa}$, where $\boldsymbol{\kappa}$ is a small deviation from a high-symmetry point $\boldsymbol{k}_0$. We consider the small deviation perturbatively and write

$$\mathcal{H} = \mathcal{H}_{\boldsymbol{k}_0} + \mathcal{H}'_{\boldsymbol{\kappa}\cdot\boldsymbol{p}}, \quad (6)$$

where

$$\mathcal{H}_{\boldsymbol{k}_0} = \frac{p^2}{m^2} + V(\boldsymbol{r}) + \frac{\hbar}{4m^2c^2}\left(\nabla V \times (\boldsymbol{p} + \boldsymbol{k}_0)\right) \cdot \boldsymbol{\sigma} \quad (7)$$

and

$$\mathcal{H}'_{\boldsymbol{\kappa}\cdot\boldsymbol{p}} = \frac{\hbar}{m}\boldsymbol{\kappa} \cdot \boldsymbol{P}. \quad (8)$$

Here, $\boldsymbol{P}$ is a generalized momentum defined as

$$\boldsymbol{P} = \left(\boldsymbol{p} + \frac{\hbar}{4mc^2}\boldsymbol{\sigma} \times \nabla V\right) \quad (9)$$

and transforms as a radial vector.

TABLE II. High-symmetry points and -lines of the conventional Brillouin zone of chalcopyrite and the little group of the wave vector. Primed symmetries are non-symmorphic and include the translation $\boldsymbol{\tau} = (0, a/2, c/4)$.

Γ	$(0,0,0)$	$E C_{2z} S_{4z}^+ S_{4z}^- C'_{2x} C'_{2y} \sigma'_{xy} \sigma'_{\bar{x}y}$
M	$(0,0,1)$	$E C_{2z} S_{4z}^+ S_{4z}^- C'_{2x} C'_{2y} \sigma'_{xy} \sigma'_{\bar{x}y}$
P	$(1/2,1/2,1/2)$	$E C_{2z} S_{4z}^+ S_{4z}^- C'_{2x} C'_{2y} \sigma'_{xy} \sigma'_{\bar{x}y}$
PA	$(1/2,1/2,-1/2)$	$E C_{2z} S_{4z}^+ S_{4z}^- C'_{2x} C'_{2y} \sigma'_{xy} \sigma'_{\bar{x}y}$
X	$(1/2,1/2,0)$	$E C_{2z} \sigma'_{xy} \sigma'_{\bar{x}y}$
N	$(1/2,0,1/2)$	$E C'_{2y}$

A. Valence band maximum

The valence band maximum is located at the X $= 2\pi(1/2a, 1/2a, 0)$ point. It is part of a two-valley structure together with X' $= 2\pi(-1/2a, 1/2a, 0)$. These points are related through symmetry transformations. Table II shows the group of the wave vector. We characterize the electron bands by double group representations. At the X-point, there are four one-dimensional irreducible representations (irreps). These couple through the radial vector $\boldsymbol{P}$ as shown in Table III.

TABLE III. Selection rules for the electronic states at the X-point.

$$\frac{\hbar}{m}\left\langle u^{X_i}\left|(P_x, P_y, P_z)\right|u^{X_i}\right\rangle = (0, 0, a_{ii})$$

$$\frac{\hbar}{m}\left\langle u^{X_2}\left|(P_x, P_y, P_z)\right|u^{X_3}\right\rangle = (a_{23}, a_{23}, 0)$$

$$\frac{\hbar}{m}\left\langle u^{X_2}\left|(P_x, P_y, P_z)\right|u^{X_4}\right\rangle = (0, 0, 0)$$

$$\frac{\hbar}{m}\left\langle u^{X_2}\left|(P_x, P_y, P_z)\right|u^{X_5}\right\rangle = (a_{25}, -a_{25}, 0)$$

$$\frac{\hbar}{m}\left\langle u^{X_3}\left|(P_x, P_y, P_z)\right|u^{X_4}\right\rangle = (a_{34}, -a_{34}, 0)$$

$$\frac{\hbar}{m}\left\langle u^{X_3}\left|(P_x, P_y, P_z)\right|u^{X_5}\right\rangle = (0, 0, 0)$$

$$\frac{\hbar}{m}\left\langle u^{X_4}\left|(P_x, P_y, P_z)\right|u^{X_5}\right\rangle = (a_{45}, a_{45}, 0)$$

Figure 3 shows that the valence band maximum consists of two nearly-degenerate bands. The upper and lower bands transform as the X_4 and X_2 irreps, respectively. They do not couple through the generalized momentum $\boldsymbol{P}$ as shown in Table III. The splitting of these bands is 10.2 meV. To describe the bands, we consider a two-band model based on Eq. (6). In deriving the secular equation, we consider second-order contributions outside the two nearly-degenerate bands. The first-order intra-band couplings are zero at band extrema.

The resulting secular equation is

$$\mathcal{H}_{2\times2}^{\mathrm{X}}\psi = E\psi, \tag{10}$$

where the two-component $\boldsymbol{\psi}$ denotes the wave function coefficients. The explicit form of the basis functions is unknown. Nevertheless, we use the transformation properties of the basis functions to derive the intra- and interband coupling parameters phenomenologically. The effective Hamiltonian $\mathcal{H}_{2\times2}^{\mathrm{X}}$ is

$$\mathcal{H}_{11} = E_2 + (A_2 + C_2)(\kappa_x^2 + \kappa_y^2) + B_2\kappa_z^2 + 2(A_2 - C_2)\kappa_x\kappa_y + \frac{\hbar^2}{2m}\kappa^2, \tag{11a}$$

$$\mathcal{H}_{12} = (M + L)(\kappa_x^2 - \kappa_y^2), \tag{11b}$$

$$\mathcal{H}_{21} = (M^* + L^*)(\kappa_x^2 - \kappa_y^2), \tag{11c}$$

$$\mathcal{H}_{22} = E_4 + (A_4 + C_4)(\kappa_x^2 + \kappa_y^2) + B_4\kappa_z^2 - 2(A_4 - C_4)\kappa_x\kappa_y + \frac{\hbar^2}{2m}\kappa^2. \tag{11d}$$

Here, E_2 and E_4 are the energies of the bands at the X-point exactly. The phenomenological parameters that govern the dispersion away from the X-point are given in Appendix C.1. The Hamiltonian $\mathcal{H}_{2\times2}^{\mathrm{X}}$ acts on a basis consisting of two wave functions transforming as the representations X_2 and X_4. These wave functions have contributions from all three types of atoms, whereas the largest contributions are from the Cu-ions. For a more intuitive understanding of these wave functions, we consider basis functions of the irreps with the relevant orbital characters. That is, we consider functions of identical transformation properties, under the little group symmetry operations, as the electron wave functions. We

present the basis functions on the form

$$\psi = |A, \boldsymbol{k}_0, O, n\rangle\begin{pmatrix}\alpha\\\beta\end{pmatrix}, \tag{12}$$

where A denotes atom type, $\boldsymbol{k}_0$ denotes the high-symmetry point, O denotes the orbital part of the wave function, and $n \in \{1, 2\}$ the location in the primitive unit cell such that $n = 1$ and $n = 2$ are related by the non-symmorphic translation. The last factor is the spinor. A similar treatment has been done for the P-point [53]. The S-ion part of the X_2 state is of p-orbital character, and the Cu-ion part is mostly of d-orbital character. The

p-orbital basis functions are of the form

$$\psi_{p_x+ip_y} = |S, X, x+iy, 1\rangle \begin{pmatrix} 1 \\ 0 \end{pmatrix}$$
$$+ e^{i\frac{3\pi}{4}} |S, X, x-iy, 2\rangle \begin{pmatrix} 0 \\ 1 \end{pmatrix}, \quad (13a)$$

$$\psi_{p_x-ip_y} = |S, X, x-iy, 1\rangle \begin{pmatrix} 1 \\ 0 \end{pmatrix}$$
$$- e^{i\frac{3\pi}{4}} |S, X, x+iy, 2\rangle \begin{pmatrix} 0 \\ 1 \end{pmatrix}, \quad (13b)$$

$$\psi_{p_z} = |S, X, z, 1\rangle \begin{pmatrix} 0 \\ 1 \end{pmatrix} + e^{\frac{3\pi}{4}i} |S, X, z, 2\rangle \begin{pmatrix} 1 \\ 0 \end{pmatrix}. \quad (13c)$$

The dominant d-orbitals are of the form

$$\psi_{d_{xz}} = |Cu, X, xz, 1\rangle \begin{pmatrix} 1 \\ 0 \end{pmatrix} + e^{\frac{\pi}{4}i} |Cu, X, yz, 2\rangle \begin{pmatrix} 0 \\ 1 \end{pmatrix}, \quad (14a)$$

$$\psi_{d_{yz}} = |Cu, X, yz, 1\rangle \begin{pmatrix} 1 \\ 0 \end{pmatrix} + e^{\frac{\pi}{4}i} |Cu, X, xz, 2\rangle \begin{pmatrix} 0 \\ 1 \end{pmatrix}, \quad (14b)$$

$$\psi_{d_{xy}} = |Cu, X, xy, 1\rangle \begin{pmatrix} 0 \\ 1 \end{pmatrix} + e^{\frac{3\pi}{4}i} |Cu, X, xy, 2\rangle \begin{pmatrix} 1 \\ 0 \end{pmatrix}. \quad (14c)$$

The non-symmorphic symmetries exchange the locations $n = 1, 2$ along with a spin-flip. The X_4 basis functions have a similar form, except that the $n = 2$ part has a relative minus sign. Evaluating the Pauli spin matrices with respect to the basis functions at the X-point reveals zero spin polarization in all directions, as consistent with the calculations shown in Figure 5.

The eigenvalues of the effective Hamiltonian in Eq. (10)

$$E_- = E_2 + (A_2 + C_2)(\kappa_x^2 + \kappa_y^2) + B_2 \kappa_z^2$$
$$+ 2(A_2 - C_2)\kappa_x \kappa_y + \frac{\hbar^2}{2m}\kappa^2, \quad (15a)$$

$$E_+ = E_4 + (A_4 + C_4)(\kappa_x^2 + \kappa_y^2) + B_4 \kappa_z^2$$
$$- 2(A_4 - C_4)\kappa_x \kappa_y + \frac{\hbar^2}{2m}\kappa^2, \quad (15b)$$

illustrate the band dispersion at the valence band maximum to second order in $\boldsymbol{\kappa}$.

The effective mass tensor is defined as

$$(m_{ij}^*)^{-1} = \frac{1}{\hbar^2}\frac{\partial^2 E}{\partial \kappa_i \partial \kappa_j} \quad (16)$$

and is, in general, valley specific. The effective mass tensor at a related valley is

$$m_{ij}^* = \mathcal{R}_{ii'}\mathcal{R}_{jj'}m_{i'j'}^* \quad (17)$$

where $\mathcal{R}$ is a symmetry transformation relating the two valleys. Now, for the two bands at the X-point, the effective masses differ in magnitude but have the same tensor form

$$m^* = \begin{pmatrix} m_{xx} & m_{xy} & 0 \\ m_{xy} & m_{xx} & 0 \\ 0 & 0 & m_{zz} \end{pmatrix}. \quad (18)$$

From numerical calculations, we estimate that

$$m_{xx}^{(4)} = -1.48, \quad m_{zz}^{(4)} = -1.36, \quad m_{xy}^{(4)} = 0.63, \quad (19a)$$

$$m_{xx}^{(2)} = -1.40, \quad m_{zz}^{(2)} = -1.37, \quad m_{xy}^{(2)} = 0.70 \quad (19b)$$

in units of the bare electron mass m. The superscripts refer to the upper X_4-band and the lower X_2-band at the valence band maximum.

B. Conduction band minimum

In this section, we consider the conduction band minimum located at the N-point. The N-point has a low symmetry and a fourfold valley degeneracy. The valleys are at N $= 2\pi(1/2a, 0, 1/2c)$, N' $= 2\pi(-1/2a, 0, 1/2c)$, N'' $= 2\pi(0, 1/2a, -1/2c)$ and N''' $= 2\pi(0, -1/2a, -1/2c)$. Each conduction band minimum consists of two non-degenerate bands. The lower band transforms as the N_4 irrep, whereas the upper band transforms as the N_3 irrep. The bands are split by 2.9 meV in the presence of SOC. We perform a similar analysis as we did for the X-point, starting with the band coupling shown in Table IV.

TABLE IV. Selection rules for electronic states at the N-point.

$\frac{\hbar}{m}\left\langle u^{N_3}\middle\| (P_x, P_y, P_z)\middle\| u^{N_3}\right\rangle = (0, a_1, 0)$
$\frac{\hbar}{m}\left\langle u^{N_4}\middle\| (P_x, P_y, P_z)\middle\| u^{N_4}\right\rangle = (0, a_2, 0)$
$\frac{\hbar}{m}\left\langle u^{N_3}\middle\| (P_x, P_y, P_z)\middle\| u^{N_4}\right\rangle = (a_{34}, 0, b_{34})$

The intra-band coupling to the first order in the crystal momentum deviation $\boldsymbol{\kappa}$ is again zero at band extrema. We find the two-band Hamiltonian

$$\mathcal{H}_{11} = E_3 + A_3\kappa_y^2 + B_3\kappa_x^2 + C_3\kappa_z^2 + (R_3 + R_3^*)\kappa_x\kappa_z + \frac{\hbar^2}{2m}\kappa^2, \tag{20a}$$

$$\mathcal{H}_{12} = a_{34}\kappa_x + b_{34}\kappa_z + (S_a + S_b)\kappa_x\kappa_y + (T_a + T_b)\kappa_y\kappa_z, \tag{20b}$$

$$\mathcal{H}_{21} = a_{34}^*\kappa_x + b_{34}^*\kappa_z + (S_a^* + S_b^*)\kappa_x\kappa_y + (T_a^* + T_b^*)\kappa_y\kappa_z, \tag{20c}$$

$$\mathcal{H}_{22} = E_4 + A_4\kappa_y^2 + B_4\kappa_x^2 + C_4\kappa_z^2 + (R_4 + R_4^*)\kappa_x\kappa_z + \frac{\hbar^2}{2m}\kappa^2. \tag{20d}$$

Here, E_3 and E_4 are the energies of the N_3 and N_4 bands at the N-point exactly. Table IV defines the first-order coupling constants a_{34} and b_{34} and the phenomenological coupling parameters to second order are defined in Appendix C.2. The corresponding eigenvalues to second order in the crystal momentum deviation $\boldsymbol{\kappa}$ are

$$
\begin{aligned}
E_+ =& E_3 + A_3\kappa_y^2 + B_3\kappa_x^2 + C_3\kappa_z^2 + (R_3 + R_3^*)\kappa_x\kappa_z \\
&+ \frac{|a_{34}|^2\kappa_x^2 + |b_{34}|^2\kappa_z^2 + (a_{34}b_{34}^* + a_{34}^*b_{34})\kappa_x\kappa_z}{E_3 - E_4} \\
&+ \frac{\hbar^2}{m^2}\kappa^2,
\end{aligned}
\tag{21a}
$$

$$
\begin{aligned}
E_- =& E_4 + A_4\kappa_y^2 + B_4\kappa_x^2 + C_4\kappa_z^2(R_4 + R_4^*)\kappa_x\kappa_z \\
&- \frac{|a_{34}|^2\kappa_x^2 + |b_{34}|^2\kappa_z^2 + (a_{34}b_{34}^* + a_{34}^*b_{34})\kappa_x\kappa_z}{E_3 - E_4} \\
&+ \frac{\hbar^2}{m^2}\kappa^2.
\end{aligned}
\tag{21b}
$$

The second-order terms in Eqs. (20b) and (20c) do not contribute to the effective mass of the bands, but to the fourth order in momentum deviation $\boldsymbol{\kappa}$. We disregard these terms.

The wave functions constituting the conduction band minimum have large Fe d_{xz} contributions. We now explore the N_3 and N_4 basis functions of this type. The basis function for the N_3 state has the form

$$\psi_{d_{xz}} = |\text{Fe}, \text{N}, xz, 1\rangle \begin{pmatrix} \alpha \\ \beta \end{pmatrix} + i\,|\text{Fe}, \text{N}, xz, 2\rangle \begin{pmatrix} \beta \\ -\alpha \end{pmatrix}. \tag{22}$$

The analogous basis function of the N_4 irrep has a relative minus sign for the $n = 2$ part. The apparent x-y asymmetry is compensated by the related valleys. The N-point has a low symmetry. Hence, the spinor part of the basis functions has a more general form than for the X-point. Evaluating the spin Pauli matrices with respect to the basis functions, we find a finite spin polarization in the y-direction consistent with Figure 5 (b).

Based on the dispersion relation of the two N-bands in Eq. (21), the effective mass tensor is of the form

$$m^* = \begin{pmatrix} m_{xx} & 0 & m_{xz} \\ 0 & m_{yy} & 0 \\ m_{xz} & 0 & m_{zz} \end{pmatrix}. \tag{23}$$

We find the numerical estimates of effective mass tensors to be

$$m_{xx}^{(4)} = 0.72, \qquad m_{yy}^{(4)} = 0.84, \tag{24a}$$

$$m_{zz}^{(4)} = 0.88, \qquad m_{xz}^{(4)} = 0.89, \tag{24b}$$

$$m_{xx}^{(3)} = 0.86, \qquad m_{yy}^{(3)} = 0.83, \tag{25a}$$

$$m_{zz}^{(3)} = 0.89, \qquad m_{xz}^{(3)} = 0.92. \tag{25b}$$

in units of the bare electron mass m. The superscripts refer to the lower N_4 state and the upper N_3 state constituting the CBM.

VI. EXTERNAL MAGNETIC FIELD

In this section, we extend the effective model for the valence electrons at the X-point and the conduction electrons at the N-point to include the effects of an external magnetic field.

We employ the Kohn-Luttinger transcription $\boldsymbol{\kappa} \to (-i\boldsymbol{\nabla} - e\boldsymbol{A})$ and account for the external magnetic field through the vector potential $\boldsymbol{A}$. This yields a system of envelope function differential equations

$$
\begin{aligned}
\sum_{n'} [D_{nn'ij}(-i\nabla_i - eA_i)&(-i\nabla_j - eA_j)] F_{n'}(\boldsymbol{r}) \\
&= EF_n(\boldsymbol{r}),
\end{aligned}
\tag{26}
$$

where F_n are envelope functions. Products of non-commuting factors should be interpreted as symmetrized products [54, 55]. To that end, we consider both the symmetric and antisymmetric terms

$$D_{nn'ij}\kappa_i\kappa_j = \frac{1}{2}D_{nn'ij}^{(S)}\{\kappa_i, \kappa_j\} + \frac{1}{2}D_{nn'ij}^{(A)}[\kappa_i, \kappa_j], \tag{27}$$

Here, $\{\kappa_i, \kappa_j\} = \kappa_i\kappa_j + \kappa_j\kappa_i$ is the anticommutator and the commutator

$$[\kappa_i, \kappa_j] = \frac{ie}{\hbar c}B_k \tag{28}$$

is finite in the presence of an external magnetic field B_k. The indices i, j, and k form a right-handed Cartesian

coordinate system. The symmetric and antisymmetric terms are defined as

$$D_{nn'ij}^{(S)} = \frac{1}{2} \left(D_{nn'ij} + D_{nn'ji} \right), \qquad (29a)$$

$$D_{nn'ij}^{(A)} = \frac{1}{2} \left(D_{nn'ij} - D_{nn'ji} \right), \qquad (29b)$$

with

$$D_{nn'ij} = \frac{\hbar^2}{2m^2} \sum_{n''} \frac{\langle n | P_i | n'' \rangle \langle n'' | P_j | n' \rangle}{E_n - E_{n''}}. \qquad (30)$$

The symmetric terms are identical to the coefficients in Eq. (11) and (20). The antisymmetric terms transform as the Zeeman coupling $H_Z = \mu_B \boldsymbol{\sigma} \cdot \boldsymbol{B}$ and give rise to an effective coupling constant g_{eff}. In general, we find that the effective Zeeman coupling tensor takes a different form than for conventional non-magnetic semiconductors. This can be understood from the form of the basis functions in Eqs. (13), (14) and (22).

For the X-point, we find

$$D_{12}^{(A)} = \mu_B \langle X_2 | \sigma_z | X_4 \rangle B_z - (M - L) \frac{ie}{\hbar c} B_z, \qquad (31a)$$

$$D_{21}^{(A)} = \mu_B \langle X_4 | \sigma_z | X_2 \rangle B_z - (M^* - L^*) \frac{ie}{\hbar c} B_z, \quad (31b)$$

where the first terms are the spin Zeeman effect and the second terms arise from coupling to external bands. Note that an external magnetic field in the xy-plane does not couple directly to the electronic states at the X-point within the regime of the two-band model. This is consistent with the form of the basis functions at the VBM.

Next, we consider the Zeeman effect and the antisymmetric terms for the N-point. We find

$$D_{11}^{(A)} = \mu_B \langle N_3 | \sigma_y | N_3 \rangle B_y - (R_3 - R_3^*) \frac{ie}{\hbar c} B_y, \qquad (32a)$$

$$\begin{aligned} D_{12}^{(A)} = &\mu_B \langle N_3 | \sigma_x | N_4 \rangle B_x + \mu_B \langle N_3 | \sigma_z | N_4 \rangle B_z \\ &- (S_a - S_b) \frac{ie}{\hbar c} B_z + (T_a - T_b) \frac{ie}{\hbar c} B_x, \end{aligned} \qquad (32b)$$

$$\begin{aligned} D_{21}^{(A)} = &\mu_B \langle N_4 | \sigma_x | N_3 \rangle B_x + \mu_B \langle N_4 | \sigma_z | N_3 \rangle B_z \\ &- (S_a^* - S_b^*) \frac{ie}{\hbar c} B_z + (T_a^* - T_b^*) \frac{ie}{\hbar c} B_x, \end{aligned} \qquad (32c)$$

$$D_{22}^{(A)} = \mu_B \langle N_4 | \sigma_y | N_4 \rangle B_y - (R_4 - R_4^*) \frac{ie}{\hbar c} B_y. \qquad (32d)$$

The N-point has a lower symmetry than the X-point. Here, the bands are split by an external magnetic field in all directions. There is a finite Zeeman coupling for each of the bands individually in the y-direction. Figure 5 (b) shows that $\langle N_3 | \sigma_y | N_3 \rangle \approx - \langle N_4 | \sigma_y | N_4 \rangle$ at the CBM.

VII. CYCLOTRON RESONANCE

The values of the effective mass tensors of the valence band maxima and the conduction band minima can be experimentally determined. One possibility is to measure the cyclotron resonance due to an AC electric field $\boldsymbol{E}$ in the presence of a static magnetic field $\boldsymbol{B}$. In this section, we investigate how the cyclotron resonance depends on the direction of the magnetic field. As discussed in section IV. B, both the VBM and CBM have a two-band structure with a splitting that appears in the presence of SOC. As shown in section V., the effective masses of these split bands differ. Hence, this structure may give rise to twice the number of resonance peaks as for a single band. The onset of the extra peaks should depend on temperature and carrier density. Consider the equation of motion

$$\frac{d(m^* \boldsymbol{v}_d)}{dt} + \frac{m^* \boldsymbol{v}_d}{\tau_m} = e(\boldsymbol{E} + [\boldsymbol{v}_d \times \boldsymbol{B}]), \qquad (33)$$

where $\boldsymbol{v}_d$ is the carrier drift velocity, m^* is the effective mass and τ_m is the scattering time [56]. To solve Eq. (33) within the many-valley model of chalcopyrite, we introduce a coordinate system $(\hat{\boldsymbol{e}}_1, \hat{\boldsymbol{e}}_2, \hat{\boldsymbol{e}}_3)$ that diagonalizes the effective mass tensor. Furthermore, we define directional cosines of the magnetic field $\boldsymbol{B}$ with respect to this coordinate system as

$$\alpha = \frac{\boldsymbol{B} \cdot \hat{\boldsymbol{e}}_1}{|\boldsymbol{B}|} \qquad \beta = \frac{\boldsymbol{B} \cdot \hat{\boldsymbol{e}}_2}{|\boldsymbol{B}|} \qquad \gamma = \frac{\boldsymbol{B} \cdot \hat{\boldsymbol{e}}_3}{|\boldsymbol{B}|}. \qquad (34)$$

These coordinates diagonalize the effective mass tensor such that

$$m^* = \begin{pmatrix} m_1 & 0 & 0 \\ 0 & m_2 & 0 \\ 0 & 0 & m_3 \end{pmatrix}. \qquad (35)$$

Eq. (33) yields $\omega_c = (e/m^*)B$ for the resonance frequency, where

$$m^* = \sqrt{\frac{m_1 m_2 m_3}{\alpha^2 m_1 + \beta^2 m_2 + \gamma^2 m_3}}. \qquad (36)$$

Here, we neglected $\boldsymbol{E}$ and τ_m^{-1} at the resonance frequency for simplicity. Both the diagonalizing coordinate system and the effective mass tensor are, in general, valley-specific. The effective mass tensors at related valleys are found from Eq. (17).

Now we consider Eq. (36) for the VBM explicitly. The effective mass tensor in Eq. (18) is diagonal in the basis

$$\hat{\boldsymbol{e}}_1 = \frac{\sqrt{2}}{2}(1, 1, 0), \quad \hat{\boldsymbol{e}}_2 = \frac{\sqrt{2}}{2}(-1, 1, 0), \quad \hat{\boldsymbol{e}}_3 = (0, 0, 1), \qquad (37)$$

with principle effective masses

$$m_1^X = m_{xx} + m_{xy}, \quad m_2^X = m_{xx} - m_{xy}, \quad m_3^X = m_{zz}, \qquad (38)$$

at the X-point. The related effective masses at X' are

$$m_1^{X'} = m_2^X, \qquad m_2^{X'} = m_1^X, \qquad m_3^{X'} = m_3^X. \qquad (39)$$

The two valleys are equivalent with respect to a magnetic field in the $\hat{z}$-direction. The effective mass in such a configuration is

$$m^* = \sqrt{m_1 m_2} = \sqrt{m_{xx}^2 - m_{xy}^2}. \qquad (40)$$

For a magnetic field, B in the xy-plane, with a polar angle θ with respect to the x-axis, the effective mass is

$$m^* = \sqrt{\frac{m_1 m_2 m_3}{m_1 \sin^2\theta + m_2 \cos^2\theta}}. \qquad (41)$$

Hence, in general, the two valleys give two distinct cyclotron resonance frequencies for an in-plane magnetic field. The number of- and the relation between the cyclotron resonance frequencies can be used to verify that the VBM is located at the X-point.

The CBMs consist of the four inequivalent N-valleys as defined in section V B. Each valley has a distinct effective mass tensor, although the tensors are related as in Eq. (17). The coordinate system in which each tensor is diagonal differs. The four sets of unit vectors are

$$\hat{e}_1 = (0, 1, 0),$$
$$\hat{e}_2 = C_- \left(\frac{m_{xx} - m_{zz} - A}{2m_{xz}}, 0, 1 \right),$$
$$\hat{e}_3 = C_+ \left(\frac{m_{xx} - m_{zz} + A}{2m_{xz}}, 0, 1 \right), \qquad (42)$$

for the N-point,

$$\hat{e}_1' = (0, 1, 0),$$
$$\hat{e}_2' = C_- \left(\frac{-m_{xx} + m_{zz} + A}{2m_{xz}}, 0, 1 \right),$$
$$\hat{e}_3' = C_+ \left(\frac{-m_{xx} + m_{zz} - A}{2m_{xz}}, 0, 1 \right). \qquad (43)$$

for the N'-point,

$$\hat{e}_1'' = (1, 0, 0),$$
$$\hat{e}_2'' = C_- \left(0, \frac{-m_{xx} + m_{zz} + A}{2m_{xz}}, 0, 1 \right),$$
$$\hat{e}_3'' = C_+ \left(0, \frac{-m_{xx} + m_{zz} - A}{2m_{xz}}, 1 \right), \qquad (44)$$

for the N''-point and

$$\hat{e}_1''' = (1, 0, 0),$$
$$\hat{e}_2''' = C_- \left(0, \frac{m_{xx} - m_{zz} - A}{2m_{xz}}, 0, 1 \right),$$
$$\hat{e}_3''' = C_+ \left(0, \frac{m_{xx} - m_{zz} + A}{2m_{xz}}, 1 \right), \qquad (45)$$

for the N'''-point. We introduced the variable $A = \sqrt{(m_{xx} - m_{zz})^2 + 4m_{xz}^2}$ for notational convenience. The normalization constants are

$$C_+ = \left(\frac{1}{2}\sqrt{4 + \left(\frac{m_{xx} - m_{zz} + A}{2m_{xz}} \right)^2} \right)^{-1}, \qquad (46a)$$

$$C_- = \left(\frac{1}{2}\sqrt{4 + \left(\frac{m_{xx} - m_{zz} - A}{2m_{xz}} \right)^2} \right)^{-1}. \qquad (46b)$$

The effective mass tensor for each valley is diagonal with respect to their coordinate system. For each of the four valleys, the diagonal elements are

$$m_1 = m_{yy}, \qquad (47a)$$
$$m_2 = \frac{1}{2}(m_{xx} + m_{zz} - A), \qquad (47b)$$
$$m_3 = \frac{1}{2}(m_{xx} + m_{zz} + A). \qquad (47c)$$

In this way, cyclotron resonance is a good way to verify the suggested multivalley structure of both the VBM and CBM.

VIII. CONCLUSIONS

$CuFeS_2$ is a semiconducting collinear antiferromagnet with a non-symmorphic crystal lattice. Its magnetic space group allows for intriguing properties such as spin-polarized electron bands and the anomalous Hall effect. We have explored its low-energy electron properties based on its magnetic symmetry group and DFT calculations. On phenomenological grounds, we found that the conductivity has components scaling linearly with the Néel vector. This included both diagonal and off-diagonal elements of the conductivity tensor. The latter corresponds to the anomalous Hall effect. The electron dispersion rendered a multivalley semiconductor with an indirect band gap of 0.779 eV. Consistent with the magnetic symmetry class, we found the electron bands to be partly spin polarized. In particular, we found an in-plane spin polarization at the conduction band minimum. We developed effective $\mathbf{k} \cdot \mathbf{p}$ models of the VBM and CBM. The resulting effective mass tensors were quantified by the *ab initio* calculations. We extended the models to include an external magnetic field using the envelope function approximation. Lastly, we suggested how to verify the effective mass tensors experimentally. The approach takes into account the multivalley band structure and serves as a framework for measuring the effective mass at and verifying the location of the determined CBM and VBM, specifically.

ACKNOWLEDGMENTS

number 262633, "QuSpin". The Norwegian Metacenter for Computational Science provided computational resources at Uninett Sigma 2, project number NN9301K. We thank B. Williamson for helpful and stimulating discussions.

Appendix A: Alternative magnetic configurations

In total, the energies of five magnetic configurations were calculated. The magnetic configurations are shown in Fig. 6. The energies of the magnetic configurations are
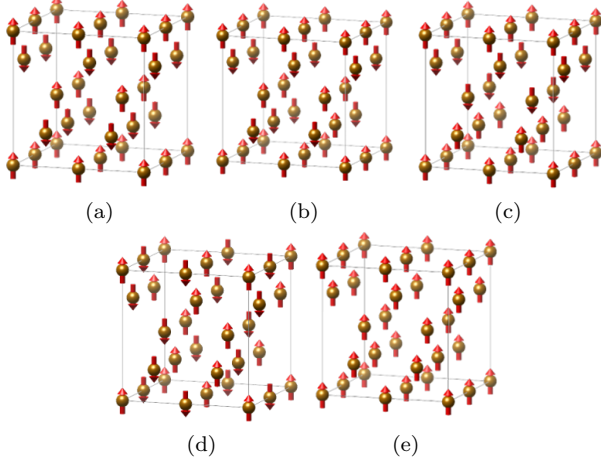
FIG. 6. Five distinct magnetic configurations of $CuFeS_2$. The configurations are of (a) A-type, (b) A′-type, (c) C-type, (d) G-type, and (e) FM-type.

given in Table V. The A-type magnetic configuration has the lowest energy and is the state considered throughout the main text.

TABLE V. Energy per formula unit of five magnetic configurations relative to that of the A-type configuration.

Type	A	A′	C	G	FM
Energy	0 meV	31.5 meV	130.1 meV	139.0 meV	54.5 meV

Appendix B: Evaluation of matrix products

We evaluate the matrix products based on the symmetry of the respective wave functions and the transformation properties of operators. As an example, we consider the matrix product

$$\langle X | \hat{O} | Y \rangle, \tag{B1}$$

where the bra state, ket state, and the operator transform as the irreducible representations Γ_X and Γ_Y, $\Gamma_{\hat{O}}$, respectively. To determine if the matrix product is finite,

we consider the corresponding tensor product

$$\Gamma_X \otimes \Gamma_{\hat{O}} \otimes \Gamma_Y = \bigoplus_i \Gamma_i, \tag{B2}$$

where the right-hand side is a direct sum of irreducible representations. The matrix product is then finite if and only if the sum on the right-hand side contains the trivial representation Γ_I. Furthermore, we can relate distinct matrix products by using that the value of all matrix products is invariant under the relevant symmetry operations.

Appendix C: Definition of free parameters

In the $\mathbf{k} \cdot \mathbf{p}$ theory, we consider the coupling between bands to second order in the $\mathcal{H}_{\boldsymbol{\kappa} \cdot \boldsymbol{p}}$ perturbation in Eq. (8). The resulting free parameters are typically treated semi-empirically. In this work, we consider them as free parameters to be determined experimentally. In the following, we define the free parameters used in section V. and VI.

1. The X-point

The X-point exhibits four distinct one-dimensional representations. We call these X_2, X_3, X_4, and X_5 consistent with the Bilbao Crystallographic Server [39].

First, we present the parameters describing the coupling between the X_2 band to all external bands

$$A_2 = \frac{\hbar^2}{m^2} \sum_{i \in Ir_3} \frac{|\langle X_2 | P_x | i \rangle|^2}{E_2 - E_i} = \frac{\hbar^2}{m^2} \sum_{i \in Ir_3} \frac{|\langle X_2 | P_y | i \rangle|^2}{E_2 - E_i}, \tag{C1}$$

$$B_2 = \frac{\hbar^2}{m^2} \sum_{i \in Ir_2} \frac{|\langle X_2 | P_z | i \rangle|^2}{E_2 - E_i}, \tag{C2}$$

$$C_2 = \frac{\hbar^2}{m^2} \sum_{i \in Ir_5} \frac{|\langle X_2 | P_x | i \rangle|^2}{E_2 - E_i} = \frac{\hbar^2}{m^2} \sum_{i \in Ir_5} \frac{|\langle X_2 | P_y | i \rangle|^2}{E_2 - E_i}. \tag{C3}$$

Here, the sums run over all bands i, which transform as the representation Ir_n. In addition, we include the processes mixing P_x, P_y, and P_z

$$A_2 = \frac{\hbar^2}{m^2} \sum_{i \in Ir_3} \frac{\langle X_2 | P_x | i \rangle \langle i | P_y | X_2 \rangle}{E_2 - E_i}, \tag{C4}$$

$$A_2 = \frac{\hbar^2}{m^2} \sum_{i \in Ir_3} \frac{\langle X_2 | P_y | i \rangle \langle i | P_x | X_2 \rangle}{E_2 - E_i}, \tag{C5}$$

$$-C_2 = \frac{\hbar^2}{m^2} \sum_{i \in Ir_5} \frac{\langle X_2 | P_x | i \rangle \langle i | P_y | X_2 \rangle}{E_2 - E_i}, \tag{C6}$$

$$-C_2 = \frac{\hbar^2}{m^2} \sum_{i \in Ir_5} \frac{\langle X_2 | P_y | i \rangle \langle i | P_x | X_2 \rangle}{E_2 - E_i}. \tag{C7}$$

Note how the non-symmorphic mirror symmetries $(\sigma_{xy}|\boldsymbol{\tau})$ and $(\sigma_{\bar{x}y}|\boldsymbol{\tau})$ relate the P_x and P_y components.

Now we consider the coupling of the X_4 band to all other bands

$$A_4 = \frac{\hbar^2}{m^2} \sum_{i\in\text{Ir}_3} \frac{|\langle X_4| P_x |i\rangle|^2}{E_4 - E_i} = \frac{\hbar^2}{m^2} \sum_{i\in\text{Ir}_3} \frac{|\langle X_4| P_y |i\rangle|^2}{E_4 - E_i}, \tag{C8}$$

$$B_4 = \frac{\hbar^2}{m^2} \sum_{i\in\text{Ir}_4} \frac{|\langle X_4| P_z |i\rangle|^2}{E_4 - E_i}, \tag{C9}$$

$$C_4 = \frac{\hbar^2}{m^2} \sum_{i\in\text{Ir}_5} \frac{|\langle X_4| P_x |i\rangle|^2}{E_4 - E_i} = \frac{\hbar^2}{m^2} \sum_{i\in\text{Ir}_5} \frac{|\langle X_4| P_y |i\rangle|^2}{E_4 - E_i}. \tag{C10}$$

The mixed-momentum components are

$$-A_4 = \frac{\hbar^2}{m^2} \sum_{i\in\text{Ir}_3} \frac{\langle X_4| P_x |i\rangle \langle i| P_y |X_4\rangle}{E_4 - E_i}, \tag{C11}$$

$$-A_4 = \frac{\hbar^2}{m^2} \sum_{i\in\text{Ir}_3} \frac{\langle X_4| P_y |i\rangle \langle i| P_x |X_4\rangle}{E_4 - E_i}, \tag{C12}$$

$$C_4 = \frac{\hbar^2}{m^2} \sum_{i\in\text{Ir}_5} \frac{\langle X_4| P_x |i\rangle \langle i| P_y |X_4\rangle}{E_4 - E_i}, \tag{C13}$$

$$C_4 = \frac{\hbar^2}{m^2} \sum_{i\in\text{Ir}_5} \frac{\langle X_4| P_y |i\rangle \langle i| P_x |X_4\rangle}{E_4 - E_i}. \tag{C14}$$

Now we consider the off-diagonal terms. That is, coupling between the X_2 and X_4 band to second order in momentum

$$M = \frac{\hbar^2}{m^2} \sum_{i\in\text{Ir}_3} \frac{\langle X_2| P_x |i\rangle \langle i| P_x |X_4\rangle}{E_4 - E_i}, \tag{C15}$$

$$-M = \frac{\hbar^2}{m^2} \sum_{i\in\text{Ir}_2} \frac{\langle X_2| P_y |i\rangle \langle i| P_y |X_4\rangle}{E_4 - E_i}, \tag{C16}$$

$$L = \frac{\hbar^2}{m^2} \sum_{i\in\text{Ir}_5} \frac{\langle X_2| P_x |i\rangle \langle i| P_x |X_4\rangle}{E_4 - E_i}, \tag{C17}$$

$$-L = \frac{\hbar^2}{m^2} \sum_{i\in\text{Ir}_5} \frac{\langle X_2| P_y |i\rangle \langle i| P_y |X_4\rangle}{E_4 - E_i}. \tag{C18}$$

Now we consider mixing of P_x, P_y and P_z terms

$$-M = \frac{\hbar^2}{m^2} \sum_{i\in\text{Ir}_3} \frac{\langle X_2| P_x |i\rangle \langle i| P_y |X_4\rangle}{E_4 - E_i}, \tag{C19}$$

$$M = \frac{\hbar^2}{m^2} \sum_{i\in\text{Ir}_3} \frac{\langle X_2| P_y |i\rangle \langle i| P_x |X_4\rangle}{E_4 - E_i}, \tag{C20}$$

$$L = \frac{\hbar^2}{m^2} \sum_{i\in\text{Ir}_5} \frac{\langle X_2| P_x |i\rangle \langle i| P_y |X_4\rangle}{E_4 - E_i}, \tag{C21}$$

$$-L = \frac{\hbar^2}{m^2} \sum_{i\in\text{Ir}_5} \frac{\langle X_2| P_y |i\rangle \langle i| P_x |X_4\rangle}{E_4 - E_i}. \tag{C22}$$

2. The N-point

In this section, we define the free parameters related to the effective description of the conduction band minimum. For each of the two bands, these are

$$A_3 = \frac{\hbar^2}{m^2} \sum_{i\in\text{Ir}_3} \frac{|\langle N_3| P_y |i\rangle|^2}{E_3 - E_i}, \tag{C23}$$

$$A_4 = \frac{\hbar^2}{m^2} \sum_{i\in\text{Ir}_4} \frac{|\langle N_4| P_y |i\rangle|^2}{E_4 - E_i}, \tag{C24}$$

$$B_3 = \frac{\hbar^2}{m^2} \sum_{i\in\text{Ir}_4} \frac{|\langle N_4| P_x |i\rangle|^2}{E_4 - E_i}, \tag{C25}$$

$$B_4 = \frac{\hbar^2}{m^2} \sum_{i\in\text{Ir}_3} \frac{|\langle N_3| P_x |i\rangle|^2}{E_3 - E_i}, \tag{C26}$$

$$C_3 = \frac{\hbar^2}{m^2} \sum_{i\in\text{Ir}_4} \frac{|\langle N_3| P_z |i\rangle|^2}{E_3 - E_i}, \tag{C27}$$

$$C_4 = \frac{\hbar^2}{m^2} \sum_{i\in\text{Ir}_3} \frac{|\langle N_4| P_z |i\rangle|^2}{E_4 - E_i} \tag{C28}$$

$$R_3 = \frac{\hbar^2}{m^2} \sum_{i\in\text{Ir}_4} \frac{\langle N_3| P_x |i\rangle \langle i| P_z |N_3\rangle}{E_3 - E_i}, \tag{C29}$$

$$R_4 = \frac{\hbar^2}{m^2} \sum_{i\in\text{Ir}_3} \frac{\langle N_4| P_x |i\rangle \langle i| P_z |N_4\rangle}{E_4 - E_i}. \tag{C30}$$

The off-diagonal coupling is captured by the free parameters

$$S_a = \frac{\hbar^2}{m^2} \sum_{i\in\text{Ir}_3} \frac{\langle N_3| P_y |i\rangle \langle i| P_x |N_4\rangle}{E_3 - E_i}, \tag{C31}$$

$$S_b = \frac{\hbar^2}{m^2} \sum_{i\in\text{Ir}_4} \frac{\langle N_3| P_x |i\rangle \langle i| P_y |N_4\rangle}{E_3 - E_i}, \tag{C32}$$

$$T_a = \frac{\hbar^2}{m^2} \sum_{i\in\text{Ir}_3} \frac{\langle N_3| P_y |i\rangle \langle i| P_z |N_4\rangle}{E_3 - E_i}, \tag{C33}$$

$$T_b = \frac{\hbar^2}{m^2} \sum_{i\in\text{Ir}_4} \frac{\langle N_3| P_z |i\rangle \langle i| P_y |N_4\rangle}{E_3 - E_i}. \tag{C34}$$

[1] T. Jungwirth, X. Marti, P. Wadley, and J. Wunderlich, Antiferromagnetic spintronics, Nat Nano **11**, 231 (2016).

[2] V. Baltz, A. Manchon, M. Tsoi, T. Moriyama, T. Ono, and Y. Tserkovnyak, Antiferromagnetic spintronics, Reviews of Modern Physics **90**, 015005 (2018).

[3] O. Gomonay, V. Baltz, A. Brataas, and Y. Tserkovnyak, Antiferromagnetic spin textures and dynamics, Nature Physics **14**, 213 (2018).

[4] P. Wadley, B. Howells, J. Železný, C. Andrews, V. Hills, R. P. Campion, V. Novák, K. Olejník, F. Maccherozzi, S. S. Dhesi, S. Y. Martin, T. Wagner, J. Wunderlich, F. Freimuth, Y. Mokrousov, J. Kuneš, J. S. Chauhan, M. J. Grzybowski, A. W. Rushforth, K. W. Edmonds, B. L. Gallagher, and T. Jungwirth, Electrical switching of an antiferromagnet, Science (2016).

[5] S. Y. Bodnar, L. Šmejkal, I. Turek, T. Jungwirth, O. Gomonay, J. Sinova, A. A. Sapozhnik, H. J. Elmers, M. Kläui, and M. Jourdan, Writing and reading antiferromagnetic Mn₂Au by Néel spin-orbit torques and large anisotropic magnetoresistance, Nature Communications **9**, 348 (2018).

[6] P. Wadley, S. Reimers, M. J. Grzybowski, C. Andrews, M. Wang, J. S. Chauhan, B. L. Gallagher, R. P. Campion, K. W. Edmonds, S. S. Dhesi, F. Maccherozzi, V. Novak, J. Wunderlich, and T. Jungwirth, Current polarity-dependent manipulation of antiferromagnetic domains, Nature Nanotechnology **13**, 362 (2018).

[7] R. Lebrun, A. Ross, S. A. Bender, A. Qaiumzadeh, L. Baldrati, J. Cramer, A. Brataas, R. A. Duine, and M. Kläui, Tunable long-distance spin transport in a crystalline antiferromagnetic iron oxide, Nature **561**, 222 (2018).

[8] Y. Tserkovnyak, A. Brataas, and G. E. W. Bauer, Enhanced gilbert damping in thin ferromagnetic films, Physical Review Letters **88**, 117601 (2002).

[9] A. Brataas, Y. Tserkovnyak, G. E. W. Bauer, and B. I. Halperin, Spin battery operated by ferromagnetic resonance, Physical Review B **66**, 060404 (2002).

[10] Y. Tserkovnyak, A. Brataas, G. E. W. Bauer, and B. I. Halperin, Nonlocal magnetization dynamics in ferromagnetic heterostructures, Reviews of Modern Physics **77**, 1375 (2005).

[11] R. Cheng, J. Xiao, Q. Niu, and A. Brataas, Spin Pumping and Spin-Transfer Torques in Antiferromagnets, Physical Review Letters **113**, 057601 (2014).

[12] Ø. Johansen and A. Brataas, Spin pumping and inverse spin hall voltages from dynamical antiferromagnets, Physical Review B **95**, 220408 (2017).

[13] J. Li, C. B. Wilson, R. Cheng, M. Lohmann, M. Kavand, W. Yuan, M. Aldosary, N. Agladze, P. Wei, M. S. Sherwin, and J. Shi, Spin current from sub-terahertz-generated antiferromagnetic magnons, Nature **578**, 70 (2020).

[14] P. Vaidya, S. A. Morley, J. van Tol, Y. Liu, R. Cheng, A. Brataas, D. Lederman, and E. del Barco, Subterahertz spin pumping from an insulating antiferromagnet, Science **368**, 160 (2020).

[15] H. Ohno, D. Chiba, F. Matsukura, T. Omiya, E. Abe, T. Dietl, Y. Ohno, and K. Ohtani, Electric-field control of ferromagnetism, Nature **408**, 944 (2000).

[16] T. Jungwirth, J. Sinova, J. Mašek, J. Kučera, and A. MacDonald, Theory of ferromagnetic (III, Mn) V semiconductors, Reviews of Modern Physics **78**, 809 (2006).

[17] M. Tanaka, Recent progress in ferromagnetic semiconductors and spintronics devices, Japanese Journal of Applied Physics **60**, 010101 (2020).

[18] T. Teranishi, Magnetic and electric properties of chalcopyrite, J. Phys. Soc. Japan **16**, 1881 (1961).

[19] L.-D. Yuan, Z. Wang, J.-W. Luo, E. I. Rashba, and A. Zunger, Giant momentum-dependent spin splitting in centrosymmetric low-Z antiferromagnets, Physical Review B **102**, 014422 (2020).

[20] L. Šmejkal, R. González-Hernández, T. Jungwirth, and J. Sinova, Crystal time-reversal symmetry breaking and spontaneous Hall effect in collinear antiferromagnets, Science Advances **6**, eaaz8809 (2020).

[21] C. Kittel, P. McEuen, and P. McEuen, *Introduction to Solid State Physics*, Vol. 8 (Wiley New York, 1996).

[22] J. Łażewski, H. Neumann, and K. Parlinski, Ab initio characterization of magnetic cufes 2, Physical Review B **70**, 195206 (2004).

[23] J. Park, Y. Xia, and V. Ozoliņš, First-principles assessment of thermoelectric properties of CuFeS₂, Journal of Applied Physics **125**, 125102 (2019).

[24] H. Takaki, K. Kobayashi, M. Shimono, N. Kobayashi, K. Hirose, N. Tsujii, and T. Mori, Seebeck coefficients in CuFeS₂ thin films by first-principles calculations, Japanese Journal of Applied Physics **58**, SIIB01 (2019).

[25] H. Takaki, K. Kobayashi, M. Shimono, N. Kobayashi, K. Hirose, N. Tsujii, and T. Mori, First-principles calculations of Seebeck coefficients in a magnetic semiconductor CuFeS₂, Applied Physics Letters **110**, 072107 (2017).

[26] M. Zhou, X. Gao, Y. Cheng, X. Chen, and L. Cai, Structural, electronic, and elastic properties of CuFeS₂: first-principles study, Applied Physics A **118**, 1145 (2015).

[27] S. Conejeros, P. Alemany, M. Llunell, I. d. P. R. Moreira, V. Sánchez, and J. Llanos, Electronic Structure and Magnetic Properties of CuFeS₂, Inorganic Chemistry **54**, 4840 (2015).

[28] R. Khaledialidusti, A. K. Mishra, and A. Barnoush, Temperature-dependent properties of magnetic CuFeS₂ from first-principles calculations: Structure, mechanics, and thermodynamics, AIP Advances **9**, 065021 (2019).

[29] T. Hamajima, T. Kambara, K. I. Gondaira, and T. Oguchi, Self-consistent electronic structures of magnetic semiconductors by a discrete variational Xα calculation. III. Chalcopyrite CuFeS₂, Physical Review B **24**, 3349 (1981).

[30] R. Edelbro, Å. Sandström, and J. Paul, Full potential calculations on the electron bandstructures of sphalerite, pyrite and chalcopyrite, Applied Surface Science **206**, 300 (2003).

[31] C. de Oliveira and H. A. Duarte, Disulphide and metal sulphide formation on the reconstructed (001) surface of chalcopyrite: A DFT study, Applied Surface Science **257**, 1319 (2010).

[32] L. Pauling and L. Brockway, The crystal structure of chalcopyrite CuFeS₂, Zeitschrift für Kristallographie-Crystalline Materials **82**, 188 (1932).

[33] G. Donnay, L. Corliss, J. Donnay, N. Elliott, and J. Hastings, Symmetry of magnetic structures: magnetic structure of chalcopyrite, Physical Review **112**, 1917 (1958).

[34] A. N. Bogdanov and D. A. Yablonski, Contribution to the theory of inhomogeneous states of magnets in the region of magnetic-field-induced phase transitions. Mixed state of antiferromagnets, Zh. Eksp. Teor. Fiz. **96**, 253 (1989).

[35] R. R. Birss, *Symmetry and magnetism*, Vol. 3 (Elsevier Science & Technology, 1966).

[36] P. E. Blöchl, Projector augmented-wave method, Physical Review B **50**, 17953–17979 (1994).

[37] G. Kresse and D. Joubert, From ultrasoft pseudopotentials to the projector augmented-wave method, Physical Review B **59**, 1758–1775 (1999).

[38] H. J. Monkhorst and J. D. Pack, Special points for Brillouin-zone integrations, Physical Review B **13**, 5188 (1976).

[39] L. Elcoro, B. Bradlyn, Z. Wang, M. G. Vergniory, J. Cano, C. Felser, B. A. Bernevig, D. Orobengoa, G. Flor, and M. I. Aroyo, Double crystallographic groups and their representations on the Bilbao Crystallographic Server, Journal of Applied Crystallography **50**, 1457 (2017).

[40] S. L. Dudarev, G. A. Botton, S. Y. Savrasov, C. J. Humphreys, and A. P. Sutton, Electron-energy-loss spectra and the structural stability of nickel oxide: An LSDA+U study, Physical Review B **57**, 1505 (1998).

[41] J. P. Perdew, A. Ruzsinszky, G. I. Csonka, O. A. Vydrov, G. E. Scuseria, L. A. Constantin, X. Zhou, and K. Burke, Restoring the Density-Gradient Expansion for Exchange in Solids and Surfaces, Phys. Rev. Lett. **100**, 136406 (2008).

[42] A. V. Krukau, O. A. Vydrov, A. F. Izmaylov, and G. E. Scuseria, Influence of the exchange screening parameter on the performance of screened hybrid functionals, J. Chem. Phys. **125**, 224106 (2006).

[43] C. H. L. Goodman and R. W. Douglas, New semiconducting compounds of diamond type structure, Physica **20**, 1107 (1954).

[44] T. E. Engin, A. V. Powell, and S. Hull, A high temperature diffraction-resistance study of chalcopyrite, CuFeS2, J. of Solid State Chem. **184**, 2272 (2011).

[45] H. C. Po, A. Vishwanath, and H. Watanabe, Symmetry-based indicators of band topology in the 230 space groups, Nature communications **8**, 1 (2017).

[46] H. Watanabe, H. C. Po, and A. Vishwanath, Structure and topology of band structures in the 1651 magnetic space groups, Science advances **4**, eaat8685 (2018).

[47] Y. Xu, L. Elcoro, Z.-D. Song, B. J. Wieder, M. Vergniory, N. Regnault, Y. Chen, C. Felser, and B. A. Bernevig, High-throughput calculations of magnetic topological materials, Nature **586**, 702 (2020).

[48] L. Elcoro, B. J. Wieder, Z. Song, Y. Xu, B. Bradlyn, and B. A. Bernevig, Magnetic topological quantum chemistry, Nature communications **12**, 1 (2021).

[49] L. C. L. Y. Voon and M. Willatzen, *The k·p Method: Electronic Properties of Semiconductors* (Springer Science & Business Media, 2009).

[50] M. S. Dresselhaus, G. Dresselhaus, and A. Jorio, *Group theory: Application to the physics of condensed matter* (Springer Science & Business Media, 2007).

[51] A. Kormányos, G. Burkard, M. Gmitra, J. Fabian, V. Zólyomi, N. D. Drummond, and V. Fal'ko, k· p theory for two-dimensional transition metal dichalcogenide semiconductors, 2D Materials **2**, 022001 (2015).

[52] M. Zhou, R. Zhang, J. Sun, W.-K. Lou, D. Zhang, W. Yang, and K. Chang, Multiband k· p theory of monolayer X Se (X= In, Ga), Physical Review B **96**, 155430 (2017).

[53] A. P. Mikhailovskii, A. M. Polubotko, V. D. Prochukhan, and Y. V. Rud, Gapless State in CuFeS2, physica status solidi (b) **158**, 229 (1990).

[54] J. M. Luttinger and W. Kohn, Motion of Electrons and Holes in Perturbed Periodic Fields, Physical Review **97**, 869 (1955).

[55] J. M. Luttinger, Quantum theory of cyclotron resonance in semiconductors: General theory, Physical review **102**, 1030 (1956).

[56] K. Seeger, *Semiconductor physics* (Springer Science & Business Media, 2013).